



# Use of Ferrocenyl Ni(II) and Zn(II) Porphyrins as Active Organic Electrode Materials for Sodium Secondary Batteries

Shaoning Zhang,<sup>[b]</sup> Jinkwang Hwang,<sup>\*[b]</sup> Quan Manh Phung,<sup>[c]</sup> Kazuhiko Matsumoto,<sup>[b]</sup> Rika Hagiwara,<sup>[b]</sup> and Ji-Young Shin<sup>\*[a]</sup>

This study investigates the potential use of ferrocenyl-substituted porphyrins as organic electrode materials for sodium secondary batteries. Expressly, 5,15-di(ferrocenyl)-10,20-di(pentafluorophenyl)porphyrins (free base, Fc–H<sub>2</sub>Por), along with its zinc (Zn[II] complex, Fc–ZnPor) and nickel (Ni[II] complex, Fc–NiPor) derivatives were synthesized and employed as the electrode materials. The charge-discharge processes disclosed that the ferrocenyl-substituted porphyrin compound performs electrochemical processes poorly without chelating metals. In contrast, when the ferrocenyl-substituted porphyrins were

metalated with Ni(II) and Zn(II), they exhibited dual ionic charge-discharge capabilities, indicating their stable electrochemical properties. In particular, long-term cycle tests emphasized the superior stability and high Coulombic efficiency of Fc–ZnPor electrodes. Computational calculations provided conclusive evidence of variances in aromatic stabilization energy based on the metal center, significantly influencing the chemical stability and electrochemical performance. These findings can deliver valuable insight for further development and optimizations in energy storage applications.

## Introduction

Rechargeable secondary batteries play a crucial role in energy storage systems in our society, especially considering the urgent global situation of demands for high-performance secondary batteries.<sup>[1]</sup> In recent years, there has been a growing focus on exploring innovative approaches to improve the performance of secondary batteries by investigating suitable electrode materials in organic compounds as their electrode materials.<sup>[2]</sup> These efforts have led to the discovery of electrode materials with desirable physiochemical and electrochemical properties, including high energy and power densities, long cyclability, low cost, and minimized decomposition reactions with the electrolyte.<sup>[3]</sup>

Porphyrins are forceful chemical structures accompanying diverse applications such as ionic traps for filtering hazardous

components,<sup>[4]</sup> anticancer drugs or drug carriers for efficient medical treatments,<sup>[5]</sup> and conducting materials for novel devices<sup>[6]</sup> due to sufficiently  $\pi$ -electron-delocalized frameworks inducing beneficial electrophysical and electrochemical properties to stabilize the progressive redox states.<sup>[7]</sup> In particular, aromatic porphyrins have gathered enormous attention from synthetic chemists and material scientists regarding the excellent merit of chemical durability, structural modification varieties with relatively calm preparation, and diverse mitigations.<sup>[8]</sup> Furthermore, various transition metal cations calmly occupy the porphyrin core, capable of stimulating durable potential catalysts for undesirable chemical reactions.<sup>[9]</sup>

Recently, we have reported exploring novel active electrode materials for secondary organic batteries using porphyrins, contracted porphyrins, and expanded porphyrins, emphasizing the battery efficiencies with long-lasting performances.<sup>[10]</sup> The norcorrole framework with 16 $\pi$ -conjugation pathways implies excellent charging and discharging performances in organic secondary batteries as a substantially active cathode electrode material, indicating the specific worth of an antiaromatic framework with innovative  $\pi$ -electronic configurations.<sup>[10d–e]</sup> Moreover, the porphyrin-based organic materials exhibited fast rate performance based on pseudocapacitive behavior associated with dual ions charge-discharge properties.<sup>[10b]</sup>

Our research on organic electrode materials has identified several primary factors crucial for achieving high-performance organic electrodes.<sup>[10]</sup> The factors include chemical durability, production of multi-redox states of the electrode materials, appropriate permeability in their solid states, and the effective stabilization of oxidation states in accord with the redox processes. Additional investigation of the different core features of porphyrins can specify their vital role in accomplishing electrochemical stability and efficiency.

In this research, ferrocenyl porphyrins were utilized as active organic electrodes for sodium secondary batteries, attempting

[a] Prof. J.-Y. Shin

Graduate School of Engineering, Nagoya University  
Huro-cho, Chikusa-ku, Nagoya, 464-8603, Japan  
E-mail: jyshin@chembio.nagoya-u.ac.jp

[b] S. Zhang, Prof. J. Hwang, Prof. K. Matsumoto, Prof. R. Hagiwara  
Graduate School of Energy Science, Kyoto University  
Yoshida-honmachi, Sakyo-ku, Kyoto, 606-8501, Japan  
E-mail: hwang.jinkwang.5c@kyoto-u.ac.jp

[c] Prof. Q. M. Phung  
Graduate School of Science  
Huro-cho, Chikusa-ku, Nagoya, 464-8602, Japan  
and  
Institute of Transformative Bio-Molecules (WPI-ITbM)  
Huro-cho, Chikusa-ku, Nagoya, 464-8602, Japan

Supporting information for this article is available on the WWW under <https://doi.org/10.1002/batt.202400004>

© 2024 The Authors. *Batteries & Supercaps* published by Wiley-VCH GmbH. This is an open access article under the terms of the Creative Commons Attribution Non-Commercial License, which permits use, distribution and reproduction in any medium, provided the original work is properly cited and is not used for commercial purposes.

to comprehend the significance of porphyrin core features. Ni(II) and Zn(II) were selectively chosen as the porphyrin metal centers. Ni(II) was the primary centering metal since the previous porphyrinoids already provided excellent outcomes with the metal. Zn(II), composing fully occupied d-orbitals with electrons, an electron-rich metal with a consistent atomic radius to fit the narrow porphyrin's core, became another selected metal center. Zn(II) complex, Fc-ZnPor, was expected to perform efficient battery behaviors induced by the charge durability during redox processes, capable of providing reliable battery behaviors to Fc-NiPor as the active electrode material. The electrochemical behavior is examined by multiple techniques and interpreted based on computational results.

## Results and Discussion

### Preparation of Ferrocenyl-Substituted Porphyrin Compounds

5,15-diferrocenyl porphyrin **2** and its metal complexes, Fc–NiPor and Fc–ZnPor, shown in Figure 1, were prepared using the methods reported in the literature. The synthesis includes acid-catalyzed condensation of pentafluorophenyl dipyrromethane **1** and ferrocene carbaldehyde in the presence of trifluoroacetic acid followed by DDD-oxidation and respective metalations.<sup>[9b,11]</sup> However, an incomplete oxidation compound **4** was isolated during the oxidation to complete  $\pi$ -conjugations for aromatic conformation. It is due to the enormously slow oxidation in  $\text{CH}_2\text{Cl}_2$ , affording the isolation of the porphyrinogen. The molecular structure was elucidated precisely by spectroscopic

and X-ray diffraction analysis methods (refer to the single crystal structure in Figure S1 and the NMR spectra in Figures S6–S8). Furthermore, the low solubilities of the reaction products in  $\text{CH}_2\text{Cl}_2$  furnished the ion pair in **5** (a deep blue fraction) to be somewhat isolable from column chromatography with gradually increased eluent's polarities with ethyl acetate (refer to the single crystal structure in Figure S2 and the NMR spectra in Figures S9–S11).

The growth of single crystals of ZnPor was succeed by a slow solvent vaporization from the  $\text{CHCl}_3$  solution. The crystal structure exhibited improved planarity associated with the tetradentate metal chelation (Figure 1b–c): Its meso-ferrocenyl groups were found to have an up-and-down orientation from the porphyrin framework in the crystal structure. Furthermore, the molecular packing stated a slipped stacking associated with the ferrocenyl exposure (Figure S3).

All proton peaks of **4** were broad in the  $^1\text{H}$  NMR spectrum shown in Figure 2a, indicating the largely flexible molecular nature. The absence of  $\pi$ -extended conjugation of **4** reveals the peaks of the  $\beta$ Hs at a nonaromatic region around 6.0 ppm. In contrast, the enhanced aromaticity through the ferrocenyl group was seen in the  $^1\text{H}$  NMR spectrum of compound **5**: Ferrocenyl-Hs shift to downfield (5.92, 5.20, and 4.26 ppm, Figure 2b), reflecting the deshielding feature.

Metal chelation can enhance the overall planarity of the porphyrin ring, whose enhanced aromaticity is supported by deshielded proton peaks in the  $^1\text{H}$  NMR spectrum. Figure 2(c–e) shows  $^1\text{H}$  NMR spectra of the porphyrin set of Fc– $\text{H}_2\text{Por}$ , Fc–ZnPor, and Fc–NiPor. Zinc(II), an ionic transition metal with a fully filled d-orbital configuration, induced stronger aromaticity of the porphyrin ring in the  $^1\text{H}$  NMR. Accomplishing a flat conformation over the porphyrin platform with the zinc complex rewarded the enhanced aromaticity. The  $\beta$ -protons for Fc–ZnPor resonate two doublets at 10.18 and 8.74 ppm (Figures 2d and S15), down-field shifted than 9.94 and 8.63 ppm of two doublets for the  $\beta$ -protons of Fc– $\text{H}_2\text{Por}$  (Figures 2c and S13). In contrast, we observed relatively upfield shifted  $\beta$ H peaks for Fc–NiPor (9.62 and 9.46 ppm). Refer to the  $^1\text{H}$  NMR

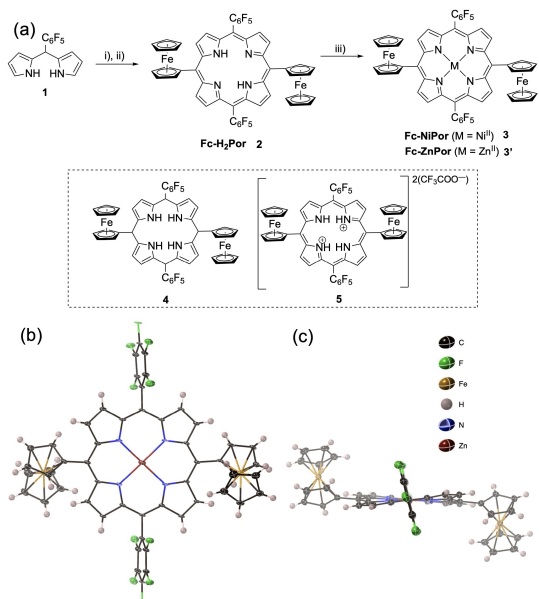


**Figure 1.** (a) Preparation of porphyrin Fc– $\text{H}_2\text{Por}$  and metal complexes Fc–NiPor and Fc–ZnPor from dipyrromethane **1**: i) ferrocene carbaldehyde/ $\text{CH}_2\text{Cl}_2$ , TFA, 0 °C, ii) DDQ iii)  $\text{Ni}(\text{acac})_2$ /toluene, reflux for Fc–NiPor (or  $\text{Zn}(\text{OAc})_2$ / $(\text{CH}_2\text{Cl}_2 + \text{MeOH})$  for Fc–ZnPor). Refer to Figures S4–S21 for the additional NMR spectra and Figures S22–S24 for the MALDI-TOF mass spectra. (b–c) Single crystal structure of Fc–ZnPor in (b) Top and (c) side views (CCDC2262760). See Table S1 for the crystallographic details.

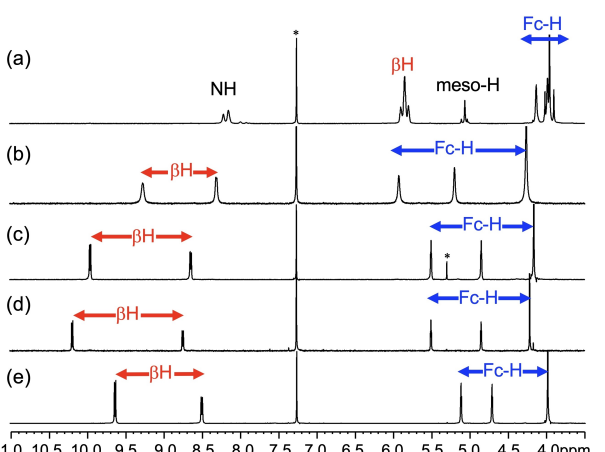


**Figure 2.**  $^1\text{H}$  NMR spectra of (a) **4**, (b) **5**, (c) Fc– $\text{H}_2\text{Por}$ , (d) Fc–ZnPor, and (e) Fc–NiPor in  $\text{CDCl}_3$ . Refer to Figures S4–S21 for the additional NMR spectra. The \* mark indicates the solvent's peak.

spectra in Figures 2e and S18 in the supporting information), elucidating a weaker aromatic electronic current than Fc–ZnPor, as informing a roofing structure over the porphyrin ring and the Ni-center.

### Electrochemical Performance

The electrochemical characteristics of the prepared ferrocenyl-substituted porphyrin compounds, Fc–H<sub>2</sub>Por, Fc–ZnPor, and Fc–NiPor, were explored using the Na[FSA]–[C<sub>2</sub>C<sub>1</sub>im][FSA] (40:60 mol%) IL electrolyte to avoid solubility in a conventional organic solvent electrolyte. The beneficial effect of the central metal elements on the charge-discharge capacity is considered to suppress either the inevitable solubility toward electrolytes with a neglectable or no solubility in the utilized IL electrolyte (Figure S26). The discharge capacities of the Fc–ZnPor and Fc–NiPor electrodes are all comparatively higher than those recorded for the Fc–H<sub>2</sub>Por electrodes (Figures 3a and S27), which shows a stable reversible capacity of 118 mAh/g of the Fc–ZnPor electrode at the 10<sup>th</sup> cycle at a current density of 200 mA/g. The charge-discharge tests were further conducted at various current densities varying from 200 to 2000 mA/g for the Fc–ZnPor electrodes. The resulting rate capability is reasonably high after the activating processes within their initial cycles, delivering the discharge capacities of 94.8 mAh/g at 500 mA/g, 76.2 mAh/g at 1000 mA/g and 61.4 mAh/g at 2000 mA/g showing the higher capacity retention of 64.4% at

the high current density of 1000 mA/g than that of the Fc–NiPor electrodes (54.1%, Figure 3b). Furthermore, the Na/Fc–ZnPor cells demonstrated stable long-term cycling performance at a high current density of 1000 mA/g, exhibiting high retention of 103% (68.2 mAh/g), 95.5% (63.0 mAh/g) and 91.4% (60.4 mAh/g) at the following 100<sup>th</sup>, 500<sup>th</sup>, and 800<sup>th</sup> cycles, respectively, with the high average Coulombic efficiency of 99.7% over 900 cycles (Figure 3c). Meanwhile, the Fc–NiPor electrodes displayed an unfavorable capacity fade in the initial cycles, with an inferior capacity retention of 57% after 800 cycles (Figures 3c and S30). SEM observation confirmed that the morphology of the Fc–ZnPor electrode after cycling is somewhat similar to the pristine morphology, maintaining precise edges and surfaces with consistent particle sizes (Figure S31). In summary, the zinc center provides rapid electrochemical storage properties with high capacity and stable cycling performance compared to the Fc–H<sub>2</sub>Por and Fc–NiPor electrodes.

To understand rapid electrochemical properties, cyclic voltammetry (CV) was performed at sweep rates ranging from 0.1 to 20.0 mV/s to examine the kinetic properties of the rapid electrochemical processes observed in the Fc-ZnPor electrode, using a sodium metal as the counter electrode (Figure S32). The total charge stored during charge-discharge cycles can be divided into two parts: the diffusion-controlled contribution derived from [FSA]<sup>-</sup> anions and Na<sup>+</sup> cations insertion/extraction and the surface-controlled contribution originating from pseudocapacitive processes. Equations S1 and S2 can quantitatively

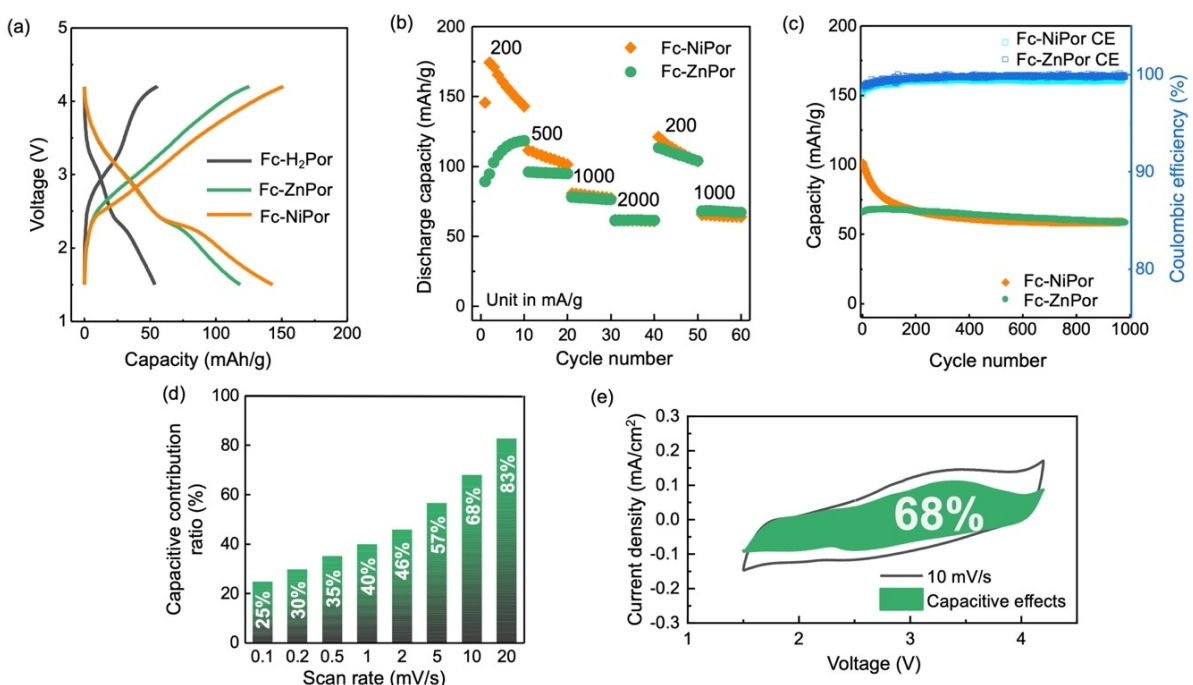


**Figure 3.** (a) The comparative charge-discharge profiles of the Fc–H<sub>2</sub>Por, Fc–ZnPor, and Fc–NiPor electrodes at a current density of 200 mA/g. Cut-off voltage: 4.2–1.5 V. The 10<sup>th</sup> cycle of each electrode is plotted. See Figure S27 for the initial charge-discharge profiles for each electrode. (b) The rate capability of the Fc–ZnPor and Fc–NiPor electrodes. Current densities: 200 to 2000 mA/g. See Figures S28 and S29 for the rate capabilities of the Fc–H<sub>2</sub>Por and the charge-discharge curves. (c) The comparative cyclability of the Fc–ZnPor and Fc–NiPor electrode. See Figure S30 for the cyclability of the Fc–H<sub>2</sub>Por electrodes. (d) The capacitive contribution of capacitive current of the Fc–ZnPor electrodes at different rates. See Figures S32–S34 and the additional comment for the CV curves and the corresponding capacitive effect evaluation at each rate of the other electrodes.

determine the capacitive ( $k_{1v}$ ) and diffusion-controlled ( $k_{2v}^{1/2}$ ) components, respectively ( $v$  denotes sweep rate).<sup>[10b]</sup> The increment on the capacitive contributions of the Fc-ZnPor electrode with increasing scan rate is shown in Figure 3d, exhibiting an increase in the capacitive contribution from 25 to 83% as the scan rate increases from 0.1 to 20 mV/s, respectively. The diffusion-controlled and surface-controlled contribution in the CV test of the Na/Fc-ZnPor cells is presented with the comparison of the total current in Figure S32 at various scan rates, where the visualized capacitive effect of 68% is shown in Figure 3e at 10 mV/s as an example, which is higher than that recorded in the Fc-H2Por electrodes with the contribution of 49% (Figure S33). This observation indicates the enhanced pseudocapacitive charge storage at high rates, further contributing to the excellent rate capability and capacity retentions obtained in the Fc-ZnPor electrodes. Similarly, a dominant capacitive behavior is observed in the Na/Fc-NiPor cell, which displays a high capacitive contribution of 81% at the sweep rate of 20 mV/s (Figure S34).

## Computational Calculations

Computation for Fc–NiPor and Fc–ZnPor resulted in similar relative free energy plots, as shown in Figures 4(a) and 4(b) (Refer to Table S2 in the supporting information). We comprehended that Ni and Zn metal centers do not participate in the redox process (refer to Figure S35 for additional discussion of XPS results for the Fc–ZnPor electrode) according to the computational data and X-ray photoelectron spectroscopy (XPS) results. In contrast, the charge-discharge mechanisms are enabled by the redox activity of ferrocenyl-substituted porphyrin rings, as previously reported.<sup>[10a–c,13b]</sup> In Fc–ZnPor, the

antibonding  $\sigma_x^{*2-y^2}$  orbital is doubly occupied; however, it is relatively low-lying due to a small contribution of the metal  $3d_x^{2-y^2}$  orbital.<sup>[14]</sup> Thus, the oxidation processes of Fc–ZnPor involve only ligand-based orbitals. To summarize, the first and second oxidation processes take place at the ferrocene moieties and require around 4.9 eV; the third and fourth oxidation processes finally yield a triplet  $\pi$  dication species. The reductions of both complexes only involve the porphyrin macrocycle, resulting in a singlet  $\pi^*$  dianion species.

Compared to the parallel structure of the nickel complex with meso-hydrogens, it is shown that the pentafluorophenyl ( $C_6F_5-$ ) substituents destabilize the cations and stabilize the anion.<sup>[15]</sup> For instance, the calculated Gibbs energy of  $[Fc-NiPor]^{4+}$  is higher than that for the neutral Fc–NiPor by 23.9 eV, whereas the corresponding value for the nickel porphyrin complex without meso-pentafluorophenyls is 23.4 eV. The stabilization of the anions is more pronounced.  $[Fc-NiPor]^{2-}$  is more stable than Fc–NiPor by 5.11 eV, whereas a corresponding value of 4.6 eV is found in the complex without meso-pentafluorophenyls. The reduction potentials of Fc–NiPor are systematically higher than those of the parallel porphyrin without meso-pentafluorophenyls.

$C_6F_5$ -substituents increase the gaps between redox states, as shown in Tables S2–S3, where we estimated the reduction potentials (versus  $Na^+/Na$ ) of Fc–NiPor and Fc–ZnPor. Figure 4 and Table S2 in the supporting information reveal that the redox properties of Fc–NiPor and Fc–ZnPor are similar. We used a value of 1.97 V (calculated at the same level of theory) for the absolute reduction potential of  $Na^+/Na$ . Although the values are qualitative and show the similarity between the oxidation processes of the two complexes, the oxidized  $[Fc-ZnPor]^{n+}$  was slightly more stable than  $[Fc-NiPor]^{n+}$ , indicating stable cycle

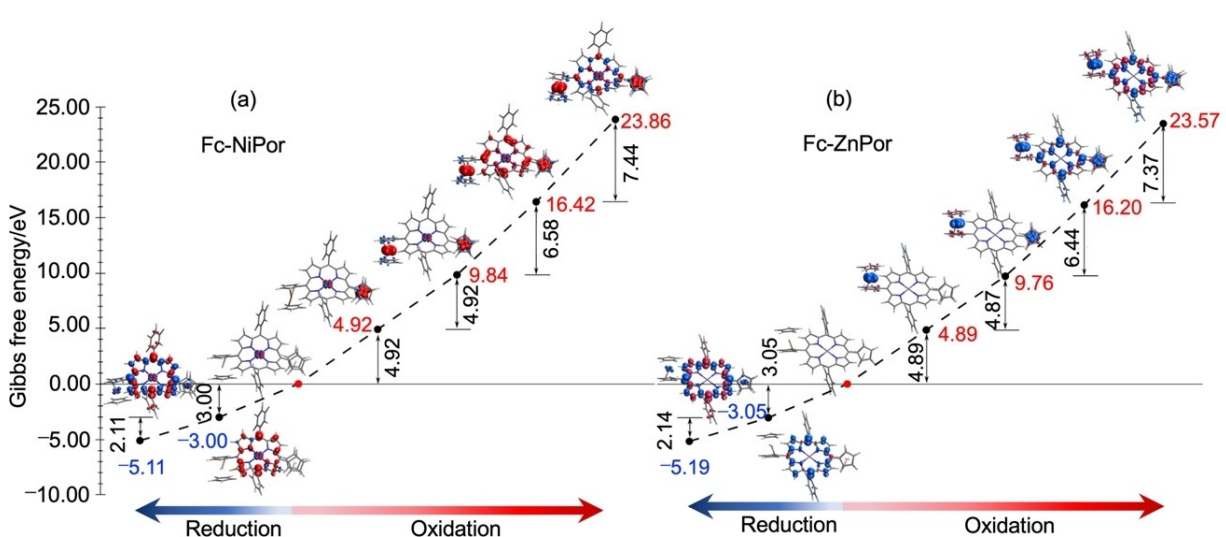


**Figure 4.** (a) Relative free energy (in eV) between  $[Fc_2(C_6F_5)_2Ni^{II}Por]^n$  and  $[Fc_2(C_6F_5)_2Ni^{IIPor}]$  for Fc–NiPor:  $n=-2, -1, +1, +2, +3, +4$ . The spin densities of the complexes are also shown, indicating the redox process can be described as  $[Fc_2(C_6F_5)_2Ni^{II}(Por^{2-})]^{2-} \rightarrow [Fc_2(C_6F_5)_2Ni^{I}(Por^{2+})] \rightarrow [Fc_2(C_6F_5)_2Ni^{II}(Por^{*+})] \rightarrow [Fc_2(C_6F_5)_2Ni^{IIPor}] \rightarrow [(Fc^{*+})(Fc)(C_6F_5)_2Ni^{IIPor}]^{4+}$  for Fc–NiPor. (b) Relative free energy (in eV) between  $[Fc_2(C_6F_5)_2Zn^{II}Por]^n$  and  $[Fc_2(C_6F_5)_2Zn^{IIPor}]$  for Fc–ZnPor:  $n=-2, -1, +1, +2, +3, +4$ . The spin densities of the complexes are also shown, indicating the redox process can be described as  $[Fc_2(C_6F_5)_2Zn^{II}(Por^{2-})]^{2-} \rightarrow [Fc_2(C_6F_5)_2Zn^{I}(Por^{2+})] \rightarrow [Fc_2(C_6F_5)_2Zn^{II}(Por^{*+})] \rightarrow [Fc_2(C_6F_5)_2Zn^{IIPor}] \rightarrow [(Fc^{*+})(Fc)(C_6F_5)_2Zn^{IIPor}]^{4+}$  for Fc–ZnPor. Calculations were done at the B3LYP-D3BJ/def2-TZVP level of theory.  $CH_2Cl_2$  solvent is used for COSMO.<sup>[12]</sup>

performance in Fc–ZnPor by suppressing inevitable reaction between electrode and electrolyte.

## Conclusions

We successfully prepared the ferrocenyl-substituted porphyrin compounds and evaluated their electrochemical properties as electrode material for secondary sodium batteries. CV analysis supported the kinetic properties, indicating those materials induce typical pseudocapacitive behavior. Significantly, the Fc–ZnPor electrodes exhibited superior rapid electrochemical charge storage properties, higher discharge capacity, and stable cycling performance compared to the Fc–H<sub>2</sub>Por and Fc–NiPor electrodes.

A stable reversible capacity of 118 mAh/g at 200 mA/g was awarded with Fc–ZnPor electrodes. The capacitive contribution of the Fc–ZnPor electrode increased from 25 to 83% as the scan rates increased from 0.1 to 20 mV/s, suggesting enhanced pseudocapacitive charge storage at high rates. Computational calculations revealed that the metal centers are not involved significantly in the redox activity. However, the battery performances highlight that the type of metal was highly concerned with electrochemical stability. The complex with Zn can efficiently stabilize the redox activity of organic ligands. The presence of pentafluorophenyl substituents destabilized the cations and stabilized the anions in the Fc–NiPor and Fc–ZnPor complexes. The practical utilization of organic electrode materials in battery systems necessitates the efficient and large-scale production of the synthetic process. Further investigation of organic electrode materials using porphyrinoid frameworks and their metal complexes is ongoing to afford fundamental background and essential knowledge in the organic electrodes for secondary batteries.

## Supporting Information

Supporting information is available from the Wiley Online Library. The authors have cited additional references within the Supporting Information.<sup>[20–22]</sup> Deposition Numbers CCDC2267193 (for compound 4), CCDC2267203 (for compound 5), and CCDC2262760 (for Fc–ZnPor) contain the supplementary crystallographic data for this paper. These data are provided free of charge by the joint Cambridge Crystallographic Data Centre and Fachinformationszentrum Karlsruhe Access Structures service.

## Acknowledgements

We acknowledge the G30 program foundation of Nagoya University for the support of this work. The computation was performed using the Research Center for Computation Science, Okazaki, Japan (Project: 23-IMS-C087). J. Shin and J. Hwang acknowledge Prof. H. Shinokubo at the Graduate School of Engineering, Nagoya University, for instrumental support.

## Conflict of Interests

The authors declare no conflict of interest.

## Data Availability Statement

The data that support the findings of this study are available in the supplementary material of this article.

**Keywords:** Electrochemical Kinetics · Porphyrin · Ferrocene · Sodium-Organic Battery · Dual-Ion Secondary Battery

- [1] a) F. Duffner, N. Kronemeyer, J. Tübke, J. Leker, M. Winter, R. Schmuck, *Nat. Energy* **2021**, *6*, 123; b) K. Roy, A. Banerjee, S. Ogale, *ACS Appl. Mater. Interfaces* **2022**, *14*, 20326; c) Y. Liu, Y. Zhu, Y. Cui, *Nat. Energy* **2019**, *4*, 540.
- [2] a) B. Esser, F. Dolhem, M. Becuwe, P. Poizot, A. Vlad, D. Brandell, *J. Power Sources* **2021**, *482*, 228814; b) J. Yang, H. Zhang, Q. Zhou, H. Qu, T. Dong, M. Zhang, B. Tang, J. Zhang, G. Cui, *ACS Appl. Mater. Interfaces* **2019**, *11*, 17109; c) T. B. Schon, B. T. McAllister, P.-F. Li, D. S. Seferos, *Chem. Soc. Rev.* **2016**, *45*, 6345; d) J. J. Shea, C. Luo, *ACS Appl. Mater. Interfaces* **2020**, *12*, 5361; e) W. Du, X. Du, M. Ma, S. Huang, X. Sun, L. Xiong, *Adv. Funct. Mater.* **2022**, *32*, 2110871; f) Y. Wang, W. Zhang, J. Yang, Y. Gong, J. Zhang, M. Fang, Q.-H. Yang, Z. Li, *Matter* **2022**, *5*, 4467; g) D. Xu, M. Liang, S. Qi, W. Sun, L.-P. Lv, F.-H. Du, B. Wang, S. Chen, Y. Wang, Y. Yu, *ACS Nano* **2021**, *15*, 47; h) Y. Liang, Y. Yao, *Joule* **2018**, *2*, 1690.
- [3] a) J. Kim, Y. Kim, J. Yoo, G. Kwon, Y. Ko, K. Kang, *Nat. Rev. Mater.* **2023**, *8*, 54; b) A. M. Battaglia, P. Pahlavanlu, E. Grignon, S. Y. An, D. S. Seferos, *ACS Appl. Mater. Interfaces* **2022**, *14*, 42298; c) C. N. Gannett, B. M. Peterson, L. Melecio-Zambrano, C. Q. Trainor, B. P. Fors, H. D. Abruña, *J. Mater. Chem. A* **2021**, *9*, 5657; d) B. M. Peterson, C. N. Gannett, L. Melecio-Zambrano, B. P. Fors, H. Abruña, *ACS Appl. Mater. Interfaces* **2021**, *13*, 7135; e) L. Huang, Y. Chen, Y. Liu, T. Wu, H. Li, J. Ye, G. Dai, X. Zhang, Y. Zhao, *ACS Sustainable Chem. Eng.* **2020**, *8*, 17868; f) F. Otteny, V. Perner, D. Wassy, M. Kolek, P. Bieker, M. Winter, B. Esser, *ACS Sustainable Chem. Eng.* **2020**, *8*, 238.
- [4] C. H. Mak, X. Han, M. Du, J.-J. Kai, K. F. Tsang, G. Jia, K.-C. Cheng, H.-H. Shen, H.-Y. Hsu, *J. Mater. Chem. A* **2021**, *9*, 4454.
- [5] S. Singh, A. Aggarwal, N. V. S. D. K. Bhupathiraju, G. Arianna, K. Tiwari, C. M. Drain, *Chem. Rev.* **2015**, *115*, 10261.
- [6] C.-C. Chen, J.-S. Chen, V. S. Nguyen, T.-C. Wei, C.-Y. Yeh, *Angew. Chem. Int. Ed.* **2021**, *60*, 4886.
- [7] G. Singh, S. Chandra, *Electrochim. Sci. Adv.* **2023**, *3*, e2100149.
- [8] *The Porphyrins: Structure and Synthesis, Part A*. Academic Press, New York, 1978.
- [9] a) *Porphyrins and Metalloporphyrin: A New Edition Based on the Original Volume* by J. E. Falk. Elsevier New York, 1975; b) A. Auger, J. C. Swarts, *Organometallics* **2007**, *26*, 102.
- [10] a) J.-Y. Shin, Z. Zhang, K. Awaga, H. Shinokubo, *Molecules* **2019**, *24*, 2433; b) J. Hwang, K. Matsumoto, R. Hagiwara, S.-Y. Liu, J.-Y. Shin, *Small Methods* **2022**, *6*, 2101181; c) J. Hwang, K. Matsumoto, R. Hagiwara, S. Ukai, H. Shinokubo, J.-Y. Shin, *Batteries & Supercaps* **2021**, *4*, 1605; d) J. Hwang, R. Hagiwara, H. Shinokubo, J.-Y. Shin, *Mater Adv* **2021**, *2*, 2263; e) J.-Y. Shin, T. Yamada, H. Yoshikawa, K. Awaga, H. Shinokubo, *Angew. Chem. Int. Ed.* **2014**, *53*, 3096.
- [11] J. S. Lindsey, *Acc. Chem. Res.* **2010**, *43*, 300.
- [12] A. Klamt, G. Schürmann, *J. Chem. Soc. Perkin Trans. 2* **1993**, 799.
- [13] a) T. C. Liu, W. G. Pell, B. E. Conway, S. L. Roberson, *J. Electrochem. Soc.* **1998**, *145*, 1882; b) S. Zhang, J. Hwang, K. Matsumoto, R. Hagiwara, ACS *Appl. Mater. Interfaces* **2022**, *14*, 19426; c) H. Lindström, S. Södergren, A. Solbrand, H. Rensmo, J. Hjelm, A. Hagfeldt, S.-E. Lindquist, *J. Phys. Chem. C* **1997**, *101*, 7717.
- [14] S. Grimme, S. Ehrlich, L. Goerigk, *J. Comput. Chem.* **2011**, *32*, 1456.
- [15] S. Zhang, J. Hwang, Q. M. Phung, K. Matsumoto, R. Hagiwara, J.-Y. Shin, *Adv. Energy Mater.* **2023**, *13*, 2301443.
- [16] a) P. J. Stephens, F. J. Devlin, C. F. Chabalowski, M. J. Frisch, *J. Phys. Chem. C* **1994**, *98*, 11623; b) S. H. Vosko, L. Wilk, M. Nusair, *Can. J. Phys.* **1980**, *58*, 1200; c) C. Lee, W. Yang, R. G. Parr, *Phys. Rev. B* **1988**, *37*, 785;

- d) A. D. Becke, *J. Chem. Phys.* **1993**, *98*, 5648; e) F. Weigend, F. Furche, R. Ahlrichs, *J. Chem. Phys.* **2003**, *119*, 12753; f) S. Grimme, J. Antony, S. Ehrlich, H. Krieg, *J. Chem. Phys.* **2010**, *132*, 154104.
- [17] S. Grimme, *Chem. Eur. J.* **2012**, *18*, 9955.
- [18] a) S. G. Balasubramani, G. P. Chen, S. Coriani, M. Diedenhofen, M. S. Frank, Y. J. Franzke, F. Furche, R. Grotjahn, M. E. Harding, C. Hättig, A. Hellweg, B. Helmich-Paris, C. Holzer, U. Huniar, M. Kaupp, A. Marefat Khah, S. Karbalaei Khani, T. Müller, F. Mack, B. D. Nguyen, S. M. Parker, E. Perlt, D. Rappoport, K. Reiter, S. Roy, M. Rückert, G. Schmitz, M. Sierka, E. Tapavicza, D. P. Tew, C. van Wüllen, V. K. Vooraa, F. Weigend, A. Wodyński, J. M. Yu, *J. Chem. Phys.* **2020**, *152*, 184107; b) R. Ahlrichs, M. Bär, M. Häser, H. Horn, C. Kölmel, *Chem. Phys. Lett.* **1989**, *162*, 165.
- [19] C.-H. Lee, J. S. Lindsey, *Tetrahedron* **1994**, *50*, 11427.
- [20] M. Namazian, C. Y. Lin, M. L. Coote, *J. Chem. Theory Comput.* **2010**, *6*, 2721.
- [21] a) J.-Y. Shin, D. Dolphin, B. O. Patrick, *Cryst. Growth Des.* **2004**, *4*, 659; b) J.-Y. Shin, B. O. Patrick, D. Dolphin, *CrystEngComm* **2008**, *10*, 960.
- [22] X. Zhang, Y. Zhou, H. Zhang, H. Li, K. Liu, H. Li, H. Pan, J. Hu, J. Fu, S. Chen, M. Liu, *J. Energy Chem.* **2021**, *63*, 625.

Manuscript received: January 4, 2024

Revised manuscript received: February 29, 2024

Accepted manuscript online: March 1, 2024

Version of record online: March 22, 2024